

# Stepped Graphene-based Aharonov-Bohm Interferometers

V. Hung Nguyen and J.-C. Charlier

*Institute of Condensed Matter and Nanosciences, Université catholique de Louvain,  
Chemin des étoiles 8, B-1348 Louvain-la-Neuve, Belgium*

Aharonov-Bohm interferences in the quantum Hall regime are observed when electrons are transmitted between two edge channels. Such a phenomenon has been realized in 2D systems such as quantum point contacts, anti-dots and  $p$ - $n$  junctions. Based on a theoretical investigation of the magnetotransport in stepped graphene, a new kind of Aharonov-Bohm interferometers is proposed herewith. Indeed, when a strong magnetic field is applied in a proper direction, oppositely propagating edge states can be achieved in both terrace and facet zones of the step, leading to the interedge scatterings and hence strong Aharonov-Bohm oscillations in the conductance in the quantum Hall regime. Taking place in the unipolar regime, this interference is also predicted in stepped systems of other 2D layered materials.

The fascinating properties of quantum hall devices arise from their ideal 1D edge states formed in a 2D electron system when a high magnetic field is applied [1, 2]. These edge states are particularly attractive due to their large coherence lengths, which is mandatory for constructing electron interferometers. However, since the edge channels are spatially separated, a mechanism for creating the electron transmission between them is required to achieve the interference effects. In this regard, one explored technique consists in building constrictions (quantum point contacts) in a sample, where the interedge tunneling paths can occur [3–17]. Setups consisting of a pair of quantum point contacts with an internal cavity has been demonstrated to work well as quantum Hall, electronic Fabry-Pérot, and Aharonov-Bohm interferometers. Another mechanism has also been suggested in systems consisting of an antidot introduced between their edges [18–25]. Electronic currents encircling the antidot can be achieved and a similar Aharonov-Bohm (AB) interference is hence observed.

Graphene, a truly 2D material, is an ideal platform for investigating quantum Hall and interference effects. Remarkably, owing to a unique linear dispersion and Dirac-like fermions [26], Landau levels and a half-integer quantum Hall effect with an unusual quantized sequence compared to the conventional systems have been observed in graphene when a strong magnetic field ( $B$ -field) is applied [27, 28]. In addition, with its semimetal character, quantum Hall systems of graphene can work in both the unipolar and bipolar regimes that can be generated and controlled by gate voltages [28–35]. Interestingly, in the bipolar regime the chiral edge states equilibration and interedge scatterings at the  $p$ - $n$  interfaces in graphene have been observed, resulting in fractional conductance plateaus [31].

With its typically high carrier mobilities, graphene is also an ideal material to perform the investigation on interference effects, including the Aharonov-Bohm one. Several experimental and theoretical observations of the AB effect in graphene nanorings have been reported (i.e., see Ref. [36] and references therein). Remarkably,

graphene  $p$ - $n$  junctions can also work as AB interferometers [32–35] in the quantum Hall regime. In particular, the oppositely propagating edge states are formed in two different doped zones and their interaction at the  $p$ - $n$  interface acquires conductance oscillations of the AB periodicity at high  $B$ -fields.

Motivated by such scientific context, a new kind of Aharonov-Bohm interferometers based on stepped graphene channels is proposed herewith. These non-planar systems have been actually achieved in several experimental situations. For example, the step bunching on the SiC surface is often observed in epitaxial graphene growth by thermal decomposition of SiC [37–

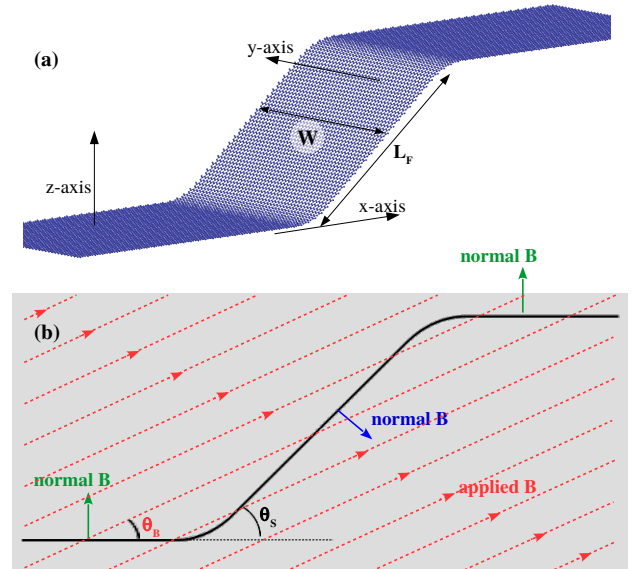


FIG. 1. Stepped graphene (a) with the ribbon width  $W$  and the length of facet zone  $L_F$ . (b) Schematic of the side view illustrating the applied magnetic field (red dashed lines of arrows) and its normal components (green and blue arrows, respectively) in both terrace and facet zones.  $\theta_B$  and  $\theta_S$  are the angles of the field and of the facet zone relative to the terrace one (Ox axis), respectively.

[47], a promising method for the production of large-area high-quality graphene. These stepped graphene channels with terrace size of several  $\mu m$  and step height of tens  $nm$  can be controllably produced by varying the heating rate [38]. Non-planar graphene systems have been also synthesized in an even better controllable way by draping graphene on pre-structured substrates [48–55].

In this work, a  $B$ -field is found to induce different effects on the electron motion in the terrace and facet zones of stepped graphene, essentially resulting from the creation of different normal components of the field in these zones. This feature has been also observed in several non-planar systems of graphene [41–47] and 2DEG [56–61], leading to anisotropic pictures when the transport takes place in the directions aligned parallel and perpendicular to the step edge. Here, a novel phenomenon is predicted when tuning the direction of  $B$ -field applied to stepped graphene. In particular, an inhomogeneous profile containing alternatively opposite normal  $B$ -components along the channel can be created, thus inducing accordingly opposite edge states. The interaction between these edge states finally results in strong AB oscillations in the quantum Hall regime as presented in this article.

The considered systems consist in graphene nanoribbons (GNRs) in the step geometry as illustrated in Fig. 1. In general, in-plane local strains can occur in the bent zones of the step, however, have been demonstrated to be small (i.e.,  $< 1\%$ ) and negligible even in epitaxial graphene [55, 62]. Moreover, such small local strains are shown not to strongly affect the predicted AB interference picture [63]. Therefore, these local strains are neglected and the  $p_z$  tight-binding Hamiltonian [26] is employed to compute the magneto-transport in this work. In particular, when a  $B$ -field is applied,

$$H = \sum_n U_n c_n^\dagger c_n + t_0 \sum_{\langle n, m \rangle} e^{i\phi_{nm}} c_n^\dagger c_m \quad (1)$$

where  $U_n$  represents the potential energy at the  $n^{th}$  site,  $t_0 = -2.7$  eV corresponds the nearest-neighbor hopping energies, and  $\phi_{nm} = \frac{e}{\hbar} \int_{\mathbf{r}_n}^{\mathbf{r}_m} \mathbf{A}(\mathbf{r}) d\mathbf{r}$  is the Peierls phase describing the effects of the  $B$ -field. Here, the magnetic field  $\mathbf{B} = B(\cos \theta_B, 0, \sin \theta_B)$  is considered by introducing the vector potential  $\mathbf{A}(\mathbf{r}) = -B(y \sin \theta_B, z \cos \theta_B, 0)$ . The above Hamiltonian is solved using the Green's-function technique [63–65], allowing for the calculation of the transport quantities perpendicular to the step edges, i.e., along the Ox axis shown in Fig. 1.

Fig. 2a displays the dependence of conductance on  $B$ -field applied in different directions in a step constituted by an armchair GNR. As mentioned, the applied  $B$ -field induces different normal components ( $B_N$ ) in the terrace and facet zones, i.e.,  $B_N = B \sin \theta_B$  (green arrows) and  $-B \sin(\theta_S - \theta_B)$  (blue arrow), respectively (see Fig. 1b). First, for  $\theta_B > \theta_S$ ,  $B_N$ -components pointing out in the

same direction are obtained, thus inducing the same propagating edge states in the two zones as illustrated in Fig. 2b. Therefore, when a large  $B$ -field is applied, a conventional Landau quantization is still obtained, i.e., the conductance represents quantized values as in Fig. 2a for  $\theta_B = 90^\circ$ . For  $\theta_B \equiv \theta_S$ , the  $B_N$ -component in the facet zone is canceled and hence the  $B$ -field has no effect on the in-plane transport in this zone. Consequently, the system behaves as a heterojunction consisting of finite- and zero-magnetic field zones and the scatterings at their interface basically explain the reduction of conductance obtained for  $\theta_B = 60^\circ \equiv \theta_S$  displayed in Fig. 2a.

Most interestingly, when  $0 < \theta_B < \theta_S$ , two opposite  $B_N$ -components alternate in the terrace and facet zones, as discussed above. Similarly to the effects of  $B$ -field in different doped zones of graphene  $p$ - $n$  junctions [31–33], opposite edge states in the terrace and facet zones are

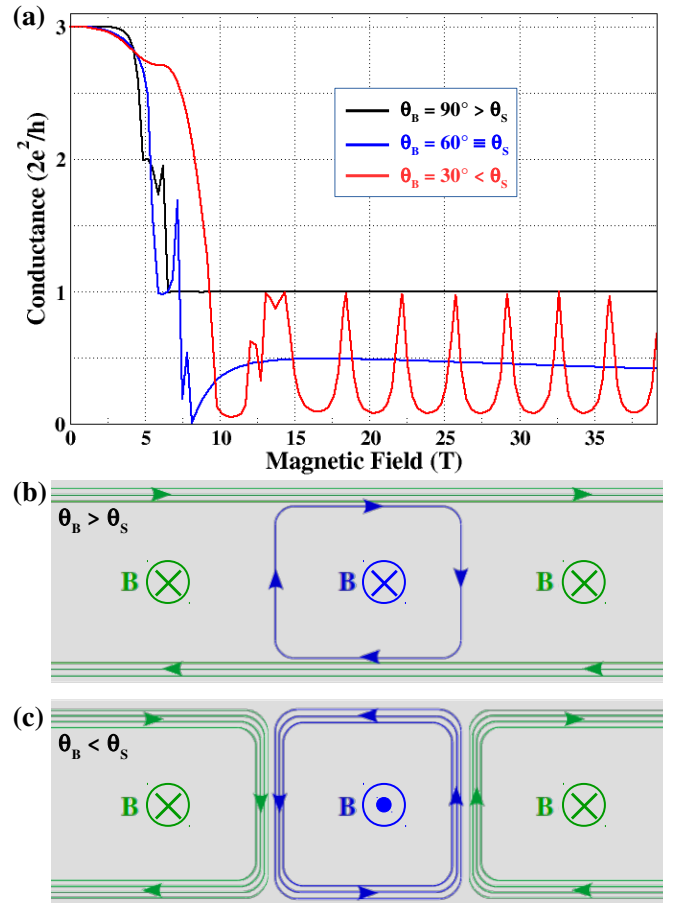


FIG. 2. (a) Conductance as a function of  $B$ -field in a stepped armchair GNR for different angles  $\theta_B$  and with  $\theta_S = 60^\circ$ ,  $E_F = 75$  meV,  $L_F \simeq 75$  nm, and  $W \simeq 40$  nm (i.e., number of dimer lines  $N_a = 324$ , a semiconducting GNR). (b,c) Diagrams illustrating the interedge scatterings for  $\theta_B > \theta_S$  and  $\theta_B < \theta_S$ , when the normal  $B$ -components in the facet and terrace zones (see Fig. 1b) are pointing out in the same and opposite directions, respectively.

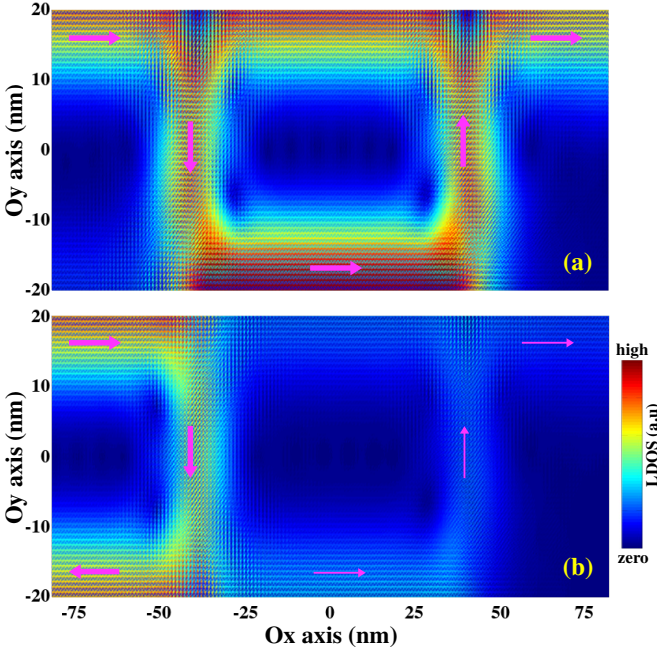


FIG. 3. Left-injected local density of states at  $B = 25.8 T$  (a) and  $27.4 T$  (b), corresponding to conductance peak and valley, respectively (see Fig. 2a for  $\theta_B = 30^\circ$ ).

created, thus inducing the strong interedge scatterings at their interface as illustrated in Fig. 2c. As an important consequence, the conductance as a function of  $B$ -field represents a strong AB oscillation in the quantum Hall regime (see the case of  $\theta_B = 30^\circ$  in Fig. 2a). This result is essentially due to the interedge backscatterings diagrammatically described in Fig. 2c and is further demonstrated by analyzing the computed left-injected local density of states in Fig. 3, that illustrates the left-to-right electron-wave propagation. Indeed, backscatterings are almost absent (Fig. 3a) when the phase coherence condition is satisfied, leading to conductance peaks. In the phase incoherence condition, strong interedge backscatterings (Fig. 3b) and hence a low conductance are achieved.

AB oscillation period observed in quantum rings with area  $S$  is known to be given by  $\Delta B = h/eS$  [66]. To examine this property in the considered systems (for  $\theta_B < \theta_S$ ), the above formula should be rewritten as

$$\Delta B = \frac{h}{eS} \frac{1}{|\sin(\theta_S - \theta_B)|} \quad (2)$$

where  $S$  is the area of the surface enclosed by the edge channel in the facet zone. Actually, the oscillation periods  $\Delta B \simeq 3.61 T$  and  $1.84 T$  are obtained in the high field regime with the facet zones of  $\sim 3000 \text{ nm}^2$  and  $6000 \text{ nm}^2$ , respectively (see Fig. 4a and additionally Figs. 2a and 4b). Indeed, the formula (2) predicts quite well these results of  $\Delta B$  if  $S \simeq 2332 \text{ nm}^2$  and  $4640 \text{ nm}^2$  are considered, which are about 22.5 % smaller than the area of the corresponding facet zones. Note that here, the edge states

are formed inside the facet zone (see Fig. 3) and hence the value of  $S$  in Eq. (2) to estimate  $\Delta B$  is basically proportional to but smaller than the area of the facet zone. Thus, the origin of observed conductance oscillation is really the AB interference due to the interaction between edge states in both terrace and facet zones.

The observed AB interference is also found to be sensitive to some other structural parameters. First, perfect armchair GNRs can be divided in two main classes with different electronic properties, either quasi-metallic with negligible bandgap or semiconducting, depending on the number of zigzag lines  $N_z$  across the ribbon width:  $N_z = 3p + 2$  and  $N_z \neq 3p + 2$  [67], respectively. Moreover, in contrast to semiconducting ribbons, the first subband of metallic GNRs is linear, thus inducing massless fermions at low energies that contribute mainly to the transport at high  $B$ -fields. As a consequence, a significant

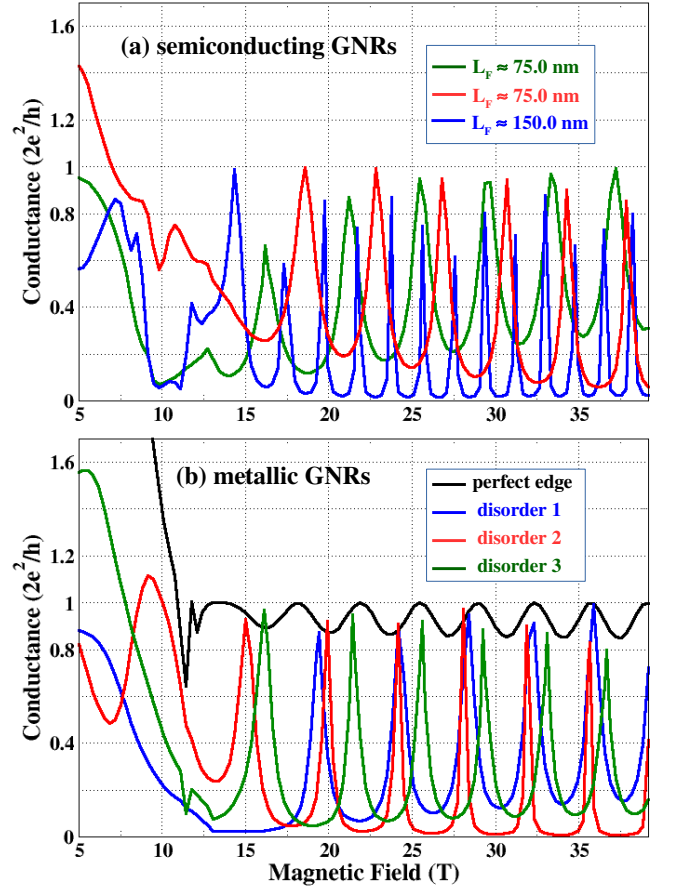


FIG. 4. (a,b) Conductance as a function of  $B$ -field at  $E_F = 75 \text{ meV}$  computed for semiconducting ( $N_z = 324$  [67]) and metallic ( $N_z = 326$ ) GNR systems, respectively, with  $\theta_S = 60^\circ$ ,  $\theta_B = 30^\circ$ , and  $W \simeq 40 \text{ nm}$ .  $L_F \simeq 75 \text{ nm}$  and  $150 \text{ nm}$  are studied in (a) while only  $L_F \simeq 75 \text{ nm}$  in (b). Except for the perfect edge in (b), different disordered configurations with the variation of ribbon width  $\delta W$  modeled by a Gaussian autocorrelation function [63], particularly, with the rsm  $W_{rsm} = 0.6 \text{ nm}$  and the correlation length  $\xi = 4.8 \text{ nm}$  are considered.



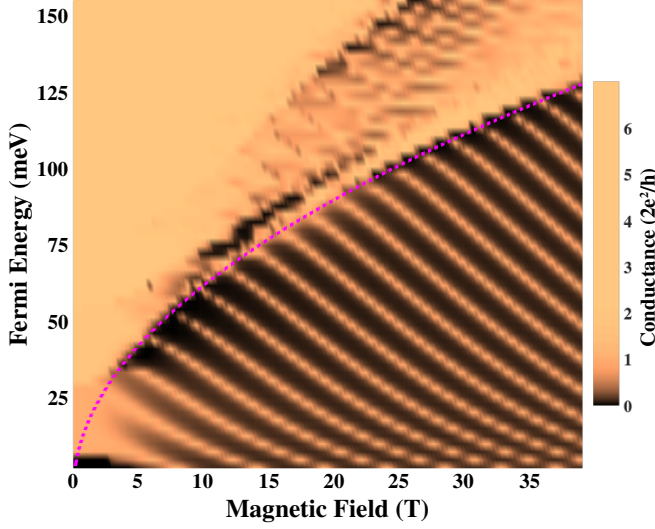


FIG. 5. Conductance map with respect to  $B$ -field and Fermi energy obtained in the system presented in Fig.2a for  $\theta_B = 30^\circ$ . The dashed line indicates the energy level  $E_1 = \min\{E_1^T, E_1^F\}$  (see text).

difference in the interference effect in the stepped systems made of these perfect GNRs is predicted. In particular, even though the conductance oscillation is similarly observed in both cases, the effect in the metallic systems (see Fig.4b for the perfect edge case) is relatively weaker than the one observed in the semiconducting GNRs (see Fig.2a for  $\theta_B = 30^\circ$ ).

Next, the effects of edge disorder, which are practically inevitable and known to degrade strongly the transport properties of GNRs [68–78], have to be evaluated. In this work, disorder is modeled (see the details in [63]) either by a Gaussian autocorrelation function (presented in Fig.4) or by randomly removing the edge atoms. The edge disorder indeed degrades significantly the transport at low fields. However, as shown in Figs.4a-b and in the Supplementary Material [63], the AB oscillations at high fields are found to be much more robust under the effect of the considered disorders than the zero-field transport. This can be explained by a fascinating feature that in the quantum Hall regime, the forward and backward edge channels are spatially separated while the scatterings at these disordered edges do not allow electrons to transmit across the sample [63], thus not inducing the strong backscatterings as at low fields. More interestingly, the edge disorder even eliminates the difference between the metallic and semiconducting GNR systems discussed above (i.e., comparison of the results obtained for perfect and disordered edges in Figs.2a and 4). Note that a picture, similar to the metallic armchair GNR case, is also observed in zigzag GNR systems, i.e., the AB oscillation is almost invisible for perfect edges but much more pronounced in edge disordered ones [63].

In Fig.5, the conductance as a function of both Fermi

energy  $E_F$  and  $B$ -field is presented. Basically, two typical zones,  $E_F \leq E_1$  and  $> E_1$ , are specified where  $E_1 = \min\{E_1^T, E_1^F\}$  with the first Landau levels  $E_1^T = \sqrt{2e\hbar v_F^2 B} |\sin \theta_B|$  and  $E_1^F = \sqrt{2e\hbar v_F^2 B} |\sin(\theta_S - \theta_B)|$  [27] formed in the terrace and facet zones, respectively, and  $v_F$  is the Fermi velocity in graphene. In particular, strong AB oscillations are predicted for  $E_F \leq E_1$  when only a single energy band is presented in both terrace and facet zones whereas the interference is blurred at higher energies. This can be explained by an inherent property of AB interference, similarly observed and demonstrated in nanoring systems [79, 80], that the strong oscillations can be observed when only a single energy band contributes to the transport, otherwise the effect can be significantly disturbed by the multi-bands contribution [63].

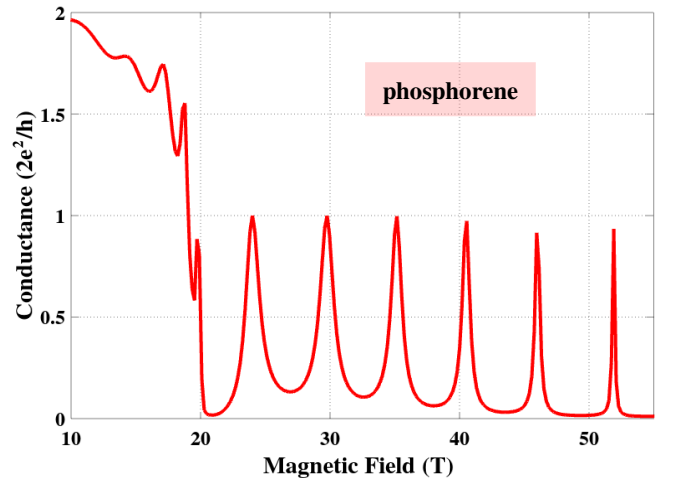


FIG. 6. Conductance as a function of  $B$ -field obtained in a stepped phosphorene system with  $\theta_S = 60^\circ$  and  $\theta_B = 30^\circ$ .  $W \simeq 40$  nm,  $L_F \simeq 110$  nm and the Fermi level is at 10 meV above the bottom of conduction bands.

It is very worth noting that the interedge scatterings in the considered structures is achieved in the unipolar regime. Therefore, different from the interference phenomena reported in graphene  $p$ - $n$  junctions, our prediction can be achieved in both cases of semi-metallic and semiconducting materials. Indeed, a similar AB interference picture is obtained in monolayer phosphorene systems by tight-binding calculations [81] and is presented in Fig. 6. Moreover, structural engineering for creating stepped structures can also allow for avoiding the junction smoothness issues, that has been shown to often perturb dramatically similar quantum phenomena in graphene  $p$ - $n$  junctions [86]. Finally, this predicted mechanism for achieving AB interferences, in principle, can be also applied to systems using ferromagnetic strips to create inhomogeneous  $B$ -fields [87], however, obtaining sharp junctions could be a practical challenge.

To conclude, the magnetotransport through stepped graphene was investigated using atomistic tight-binding

calculations. By applying the  $B$ -field in a proper direction, opposite normal components of the field can be created, thus inducing opposite edge states, in the terrace and facet zones. The interedge scatterings were observed, leading to strong Aharonov-Bohm oscillations in the quantum Hall regime. The properties of this interference, depending on the carrier energy and structural parameters, were systematically clarified. Moreover, since it is observed in the unipolar regime, our prediction can be also achieved in stepped systems made of other (both semimetallic and semiconducting) 2D layered materials.

**Acknowledgments** - We acknowledge financial support from the F.R.S.-FNRS of Belgium through the research project (N° T.1077.15), from the Flag-Era JTC 2017 project "MECHANIC" (N° R.50.07.18.F), from the Fédération Wallonie-Bruxelles through the ARC on 3D nanoarchitecturing of 2D crystals (N° 16/21-077) and from the European Union's Horizon 2020 research and innovation program (N° 696656).

- 
- [1] K. von Klitzing, *Rev. Mod. Phys.* **58**, 519-531 (1986).
  - [2] David K. Ferry (IOP Publishing, 2015) p. 6.1 to 6.26.
  - [3] B. W. Alphenaar, A. A. M. Staring, H. van Houten, M. A. A. Mabeoone, O. J. A. Buyk, and C. T. Foxon, *Phys. Rev. B* **46**, 7236-7239 (1992).
  - [4] C. de C. Chamon, D. E. Freed, S. A. Kivelson, S. L. Sondhi, and X. G. Wen, *Phys. Rev. B* **55**, 2331-2343 (1997).
  - [5] B. I. Halperin, A. Stern, I. Neder, and B. Rosenow, *Phys. Rev. B* **83**, 155440 (2011).
  - [6] P. Bonderson, A. Kitaev, and K. Shtengel, *Phys. Rev. Lett.* **96**, 016803 (2006).
  - [7] P. Bonderson, K. Shtengel, and J. K. Slingerland, *Phys. Rev. Lett.* **97**, 016401 (2006).
  - [8] A. Stern and B. I. Halperin, *Phys. Rev. Lett.* **96**, 016802 (2006).
  - [9] R. Ilan, E. Grosfeld, K. Schoutens, and A. Stern, *Phys. Rev. B* **79**, 245305 (2009).
  - [10] F. E. Camino, W. Zhou, and V. J. Goldman, *Phys. Rev. B* **76**, 155305 (2007).
  - [11] F. E. Camino, W. Zhou, and V. J. Goldman, *Phys. Rev. Lett.* **98**, 076805 (2007).
  - [12] Y. Zhang, D. T. McClure, E. M. Levenson-Falk, C. M. Marcus, L. N. Pfeiffer, and K. W. West, *Phys. Rev. B* **79**, 241304 (2009).
  - [13] D. T. McClure, Y. Zhang, B. Rosenow, E. M. Levenson-Falk, C. M. Marcus, L. N. Pfeiffer, and K. W. West, *Phys. Rev. Lett.* **103**, 206806 (2009).
  - [14] P. V. Lin, F. E. Camino, and V. J. Goldman, *Phys. Rev. B* **80**, 125310 (2009).
  - [15] N. Ofek, A. Bid, M. Heiblum, A. Stern, V. Umansky, and D. Mahalu, *Proc. Natl. Acad. Sci. USA* **107**, 5276-5281 (2010).
  - [16] D. T. McClure, W. Chang, C. M. Marcus, L. N. Pfeiffer, and K. W. West, *Phys. Rev. Lett.* **108**, 256804 (2012).
  - [17] R. Sabo, I. Gurman, A. Rosenblatt, F. Lafont, D. Banitt, J. Park, M. Heiblum, Y. Gefen, V. Umansky, and D. Mahalu, *Nat. Phys.* **13**, 491-496 (2017).
  - [18] M. Kataoka, C. J. B. Ford, G. Faini, D. Mailly, M. Y. Simmons, and D. A. Ritchie, *Phys. Rev. B* **62**, R4817-R4820 (2000).
  - [19] H.-S. Sim, M. Kataoka, Hangmo Yi, N. Y. Hwang, M.-S. Choi, and S.-R. Eric Yang, *Phys. Rev. Lett.* **91**, 266801 (2003).
  - [20] S. Ihnatsenka, I. V. Zozoulenko, and G. Kirczenow, *Phys. Rev. B* **80**, 115303 (2009).
  - [21] H.-S. Sim, M. Kataoka, and C.J.B. Ford, *Phys. Rep.* **456**, 127-165 (2008).
  - [22] B. Hackens, F. Martins, S. Faniel, C.A. Dutu, H. Sellier, S. Huant, M. Pala, L. Desplanque, X. Wallart, and V. Bayot, *Nat. Commun.* **1**, 39 (2010).
  - [23] N. Paradiso, S. Heun, S. Roddaro, G. Biasiol, L. Sorba, D. Venturelli, F. Taddei, V. Giovannetti, and F. Beltram, *Phys. Rev. B* **86**, 085326 (2012).
  - [24] F. Martins, S. Faniel, B. Rosenow, M. G. Pala, H. Sellier, S. Huant, L. Desplanque, X. Wallart, V. Bayot, and B. Hackens, *New J. Phys.* **15**, 013049 (2013).
  - [25] L. S. Sarah, S. Ady, R. Bernd, and I. H. Bertrand, *Physica E* **76**, 82-87 (2016).
  - [26] A. H. Castro Neto, F. Guinea, N. M. R. Peres, K. S. Novoselov, and A. K. Geim, *Rev. Mod. Phys.* **81**, 109-162 (2009).
  - [27] L.-J. Yin, K.-K. Bai, W.-X. Wang, S.-Y. Li, Y. Zhang, and L. He, *Front. Phys.* **12**, 127208 (2017).
  - [28] T. Machida, S. Morikawa, S. Masubuchi, R. Moriya, M. Arai, K. Watanabe, and T. Taniguchi, *J. Phys. Soc. Jpn.* **84**, 121007 (2015).
  - [29] D. A. Abanin and L. S. Levitov, *Science* **317**, 641-643 (2007).
  - [30] J. R. Williams, L. DiCarlo, and C. M. Marcus, *Science* **317**, 638-641 (2007).
  - [31] B. Özyilmaz, P. Jarillo-Herrero, D. Efetov, D. A. Abanin, L. S. Levitov, and P. Kim, *Phys. Rev. Lett.* **99**, 166804 (2007).
  - [32] S. Morikawa, S. Masubuchi, R. Moriya, K. Watanabe, T. Taniguchi, and T. Machida, *Appl. Phys. Lett.* **106**, 183101 (2015).
  - [33] A. Mreńca-Kolasińska, S. Heun, and B. Szafran, *Phys. Rev. B* **93**, 125411 (2016).
  - [34] D. S. Wei, T. van der Sar, J. D. Sanchez-Yamagishi, K. Watanabe, T. Taniguchi, P. Jarillo-Herrero, B. I. Halperin, and A. Yacoby, *Sci. Adv.* **3**, e1700600 (2017).
  - [35] P. Makk, C. Handschin, E. Tóvári, K. Watanabe, T. Taniguchi, K. Richter, M.-H. Liu, and C. Schönenberger, *Phys. Rev. B* **98**, 035413 (2018).
  - [36] S. Jorg, R. Patrik, and T. Bjorn, *Sol. State Commun.* **152**, 1411-1419 (2012).
  - [37] F. Giannazzo, I. Deretzis, G. Nicotra, G. Fisichella, C. Spinella, F. Roccaforte, and A. La Magna, *Appl. Surf. Sci.* **291**, 53-57 (2014).
  - [38] J. Bao, O. Yasui, W. Norimatsu, K. Matsuda, and M. Kusunoki, *Appl. Phys. Lett.* **109**, 081602 (2016).
  - [39] F. Speck, M. Ostler, S. Besenfelder, J. Krone, M. Wanke, and T. Seyller, *Ann. Phys.* **529**, 1700046 (2017).
  - [40] A. Stöhr *et al.*, *Ann. Phys.* **529**, 1700052 (2017).
  - [41] S. Odaka, H. Miyazaki, S.-L. Li, A. Kanda, K. Morita, S. Tanaka, Y. Miyata, H. Kataura, K. Tsukagoshi, and Y. Aoyagi, *Appl. Phys. Lett.* **96**, 062111 (2010).
  - [42] H. Kuramochi, S. Odaka, K. Morita, S. Tanaka, H. Miyazaki, M. V. Lee, S.-L. Li, H. Hiura, and K. Tsukagoshi, *AIP Advances* **2**, 012115 (2012).

- [43] T. Schumann, K.-J. Friedland, M. H. Oliveira, A. Tahraoui, J. M. J. Lopes, and H. Riechert, *Phys. Rev. B* **85**, 235402 (2012).
- [44] E. Pallecchi, E. Lafont, V. Cavaliere, F. Schopfer, D. Mailly, W. Poirier, and A. Ouerghia, *Sci. Rep.* **4**, 4558 (2014).
- [45] T. Ciuk, S. Cakmakyapan, E. Ozbay, P. Caban, K. Grodecki, A. Krajewska, I. Pasternak, J. Szmids, and W. Strupinski, *J. Appl. Phys.* **116**, 123708 (2014).
- [46] E. Akira, K. Fumio, M. Kouhei, K. Takashi, and T. Satoru, *J. Low Temp. Phys.* **179**, 237-250 (2015).
- [47] D. Momeni Pakdehi *et al.*, *ACS Appl. Mater. Interfaces* **10**, 6039-6045 (2018).
- [48] T. Takahiro and O. Toshio, *Carbon* **50**, 674-679 (2012).
- [49] H. Kenjiro, S. Shintaro, and Y. Naoki, *Nanotechnol.* **24**, 025603 (2012).
- [50] J.-K. Lee *et al.*, *Nano Lett.* **13**, 3494-3500 (2013).
- [51] C.-H. Lee *et al.*, *Adv. Mater.* **26**, 2812-2817 (2014).
- [52] M. E. Ayhan, G. Kalita, M. Kondo, and M. Tanemura, *RSC Adv.* **4**, 26866-26871 (2014).
- [53] S. Dai *et al.*, *Nat. Nanotechnol.* **10**, 682-686 (2015).
- [54] K.-K. Bai, J.-B. Qiao, H. Jiang, H. Liu, and L. He, *Phys. Rev. B* **95**, 201406 (2017).
- [55] B. D. Briggs *et al.*, *Appl. Phys. Lett.* **97**, 223102 (2010).
- [56] M. L. Leadbeater, C. L. Foden, J. H. Burroughes, M. Pepper, T. M. Burke, L. L. Wang, M. P. Grimshaw, and D. A. Ritchie, *Phys. Rev. B* **52**, R8629-R8632 (1995).
- [57] M. L. Leadbeater, C. L. Foden, J. H. Burroughes, T. M. Burke, L. L. Wang, M. P. Grimshaw, D. A. Ritchie, and M. Pepper, *Surf. Sci.* **361/362**, 587-590 (1996).
- [58] I. S. Ibrahim, V. A. Schweigert, and F. M. Peeters, *Phys. Rev. B* **56**, 7508 (1997).
- [59] S. Cinà, D. M. Whittaker, D. D. Arnone, T. Burke, H. P. Hughes, M. Leadbeater, M. Pepper, and D. A. Ritchie, *Phys. Rev. Lett.* **83**, 4425-4428 (1999).
- [60] A. Nauen, U. Zeitler, R. J. Haug, A. G. M. Jansen, M. Dilger, and K. Eberl, *Physica E* **13**, 732-735 (2002).
- [61] M. Grayson, D. Schuh, M. Bichler, M. Huber, G. Abstreiter, L. Hoepfel, J. Smet, and K. von Klitzing, *Physica E* **22**, 181-184 (2004).
- [62] J. A. Robinson, C. P. Puls, N. E. Staley, J. P. Stitt, M. A. Fanton, K. V. Emtsev, T. Seyller and Y. Liu, *Nano Lett.* **9**, 964-968 (2009).
- [63] See Supplemental Material, which includes Refs. [27, 33, 55, 62, 64, 65, 68-80, 82-85]. In this material, computational methodologies, effects of local strains, edge disorders, and multi-bands contribution are presented in detail.
- [64] V. Hung Nguyen, J. Saint-Martin, D. Querlioz, F. Mazamuto, A. Bournel, Y.-M. Niquet, and P. Dollfus, *J. Comput. Electron.* **12**, 85-93 (2013).
- [65] C. H. Lewenkopf and E. R. Mucciolo, *J. Comput. Electron.* **12**, 203-231 (2013).
- [66] Y. Aharonov and D. Bohm, *Phys. Rev.* **115**, 485-491 (1959).
- [67] Armchair GNRs with perfect edges can be basically divided in two main classes, depending on the number of zigzag lines  $N_z$  across their width, i.e., GNRs with  $N_z = 3p + 2$  are metallic while they are semiconducting in the other cases. The details can be found in Y.-W. Son *et al.*, *Phys. Rev. Lett.* **97**, 216803 (2016) or in S. M.-M. Dubois *et al.*, *Eur. Phys. J. B* **72**, 1-24 (2009).
- [68] M. Y. Han, B. zyilmaz, Y. Zhang, and P. Kim, *Phys. Rev. Lett.* **98**, 206805 (2007).
- [69] M. Y. Han, J. C. Brant, and P. Kim, *Phys. Rev. Lett.* **104**, 056801 (2010).
- [70] M. V. Fischetti and S. Narayanan, *J. Appl. Phys.* **110**, 083713 (2011).
- [71] N. Djavid *et al.*, *IEEE Trans. Electron Devices* **61**, 23 - 29 (2014).
- [72] T. Misawa *et al.*, *Jpn. J. Appl. Phys.* **54**, 05EB01 (2015).
- [73] T. Fang, A. Konar, H. Xing, and D. Jena, *Phys. Rev. B* **78**, 205403 (2008).
- [74] A. Y. Goharizi *et al.*, *IEEE Trans. Electron Devices* **58**, 3725 - 3735 (2011).
- [75] M. Evaldsson *et al.*, *Phys. Rev. B* **78**, 161407(R) (2008).
- [76] D. Querlioz *et al.*, *Appl. Phys. Lett.* **92**, 042108 (2008).
- [77] M. Poljak and T. Suligoj, *IEEE Trans. Electron Devices* **63**, 537-543 (2016).
- [78] A. Cresti and S. Roche, *New J. Phys.* **11**, 095004 (2009).
- [79] V. Hung Nguyen, Y. M. Niquet, and P. Dollfus, *Phys. Rev. B* **88**, 035408 (2013).
- [80] R. Zhang, Z. Wu, X. J. Li, and K. Chang, *Phys. Rev. B* **95**, 125418 (2017).
- [81] A. N. Rudenko and M. I. Katsnelson, *Phys. Rev. B* **89**, 201408 (2014).
- [82] Y. Xu, H. Gao, M. Li, Z. Guo, H. Chen, Z. Jin and B. Yu, *Nanotechnol.* **22**, 365202 (2011).
- [83] T. Low, V. Perebeinos, J. Tersoff, and Ph. Avouris, *Phys. Rev. Lett.* **108**, 096601 (2012).
- [84] <http://www.openmx-square.org>.
- [85] V. M. Pereira, A. H. Castro Neto, and N. M. R. Peres, *Phys. Rev. B* **80**, 045401 (2009).
- [86] V. V. Cheianov and V. I. Fal'ko, *Phys. Rev. B* **74**, 041403(R) (2006).
- [87] A. Nogaret, *J. Phys.: Condens. Matter* **22**, 253201 (2010).

# Supplemental material for “Stepped Graphene-based Aharonov-Bohm Interferometers”

**V. Hung Nguyen and J.-C. Charlier**

*Institute of Condensed Matter and Nanosciences, Université catholique de Louvain,  
Chemin des étoiles 8, B-1348 Louvain-la-Neuve, Belgium*

## Contents:

1. **Computational methodologies**
  2. **Curvature-induced local strains in stepped graphene**  
*Local strains induced by curvature and simulated models are discussed.*
  3. **Tight Binding versus Density Functional Theory calculations**  
*Validity of tight binding model to investigate the local strains is considered by the fit to the density functional theory calculations*
  4. **Effects of curvature-induced local strains on Aharonov-Bohm interference**
  5. **Effects of edge disorder in graphene nanoribbons**
  6. **Multi sub-bands contribution**  
*References*
- 

## 1. Computational methodologies

In order to compute the electronic transport through stepped graphene systems, we employed the Green's function technique [1] to solve the tight-binding Hamiltonian presented in the main text. In particular, the retarded Green's function is determined as

$$G^R(E) = [E + i0^+ - H_D - \Sigma_L - \Sigma_R]^{-1} \quad (\text{S.1})$$

where  $H_D$  is the device Hamiltonian and  $\Sigma_{L,R}$  are self-energies describing the left and right device-to-lead couplings, respectively. This equation was solved using the recursive method [2]. The transport quantities such as transmission probability  $T(E)$ , conductance  $\mathcal{G}(E_F)$  and local density of left- and right-injected states  $D_{L,R}(E, r)$  are then computed using the Landauer formalism as follows:

$$T(E) = \text{Tr}[\Gamma_L G^R \Gamma_R G^{R\dagger}] \quad (\text{S.2})$$

$$\mathcal{G}(E_F) = \frac{2e^2}{h} \int_{-\infty}^{+\infty} dE T(E) \left( -\frac{\partial f_F}{\partial E} \right) \quad (\text{S.3})$$

$$D_{L,R}(E, r) = \frac{G^R \Gamma_{L,R} G^{R\dagger}}{2\pi} \quad (\text{S.4})$$

Here,  $\Gamma_{L,R} = i[\Sigma_{L,R} - \Sigma_{L,R}^\dagger]$  and  $f_F(E)$  is the Fermi-Dirac distribution function with the Fermi level  $E_F$ . The total local density of states can be computed either by  $D(E, r) = D_L(E, r) + D_R(E, r)$  or  $D(E, r) = -\Im(G^R)/\pi$ .

## 2. Curvature-induced local strains in stepped graphene

In general, the non-planar geometry can induce in-plane strain inhomogeneities (i.e., local strains). Different from the uniform strains, local strains can result in electron scatterings and can be effectively described as the effects of strain-induced gauge fields in stepped graphene systems. These local strains have been shown to be often observed in the detached regions, i.e., around the step edges [3-5].

However, it has been experimentally demonstrated that if no external stress is applied, only small local strains can be observed in the stepped graphene systems, because of the mechanical robustness of graphene layers. For instance, it has been investigated and reported in refs. [3,4] that graphene at the step could experience small uniaxial strains (i.e.,  $< 1\%$ ) relative to the rest of the sheet and **nearly strain-free graphene is possible in epitaxial graphene**. Extremely small strains of  $\sim 0.025\%$  were also demonstrated in ref. [5] by Raman spectroscopy measurements.

To investigate the effects of such local strains induced by graphene curvature, we assume a simple model that the strain is maximum at the step edges and gradually release in two sides. Here, we use the following simple formula to model these strains:

$$\varepsilon(r) = \frac{\varepsilon_{\max}}{1 + (d/d_0)^2} \quad (\text{S.5})$$

where  $\varepsilon_{\max}$  is the maximum value of strain,  $d$  is the in-plane distance from the position  $\mathbf{r}$  to the considered step edge, and  $d_0$  characterizes the strain release distance. Fig. S1 shows a typical picture of possible strain gradients induced by graphene curvature, that can be modelled by the above formula.

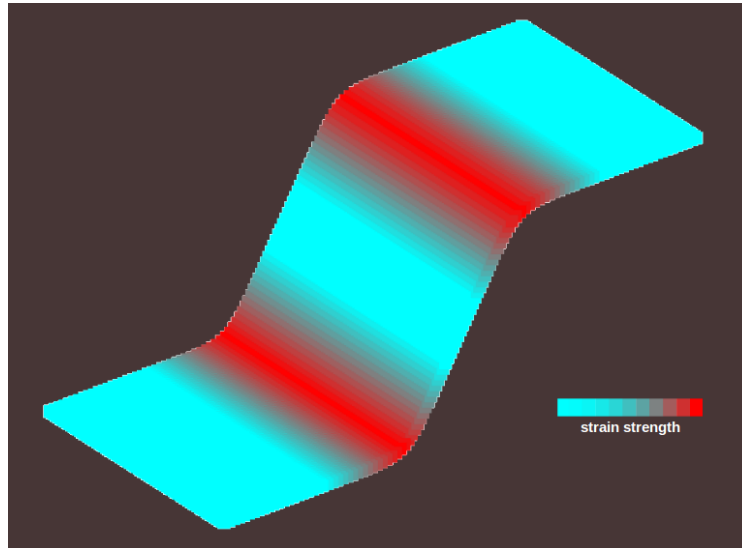


**Fig. S1:** Possible local strains induced by curvature in stepped graphene systems.

In next sections 3 and 4, using such the simple model we present an investigation to clarify the effects of possible local strains mentioned above on the Aharonov-Bohm interference predicted in this work.



### 3. Tight Binding versus Density Functional Theory calculations

In this section, we present some calculations demonstrating the validity of the tight binding (TB) Hamiltonian to investigate the curvature-induced local strains in stepped graphene systems by the fit to the *ab initio* quantum transport data [6].

Actually, it has been shown by several studies in the literature that a simple  $p_z$  TB Hamiltonian with only nearest neighbor interactions can be used to compute very accurately the electronic properties and electron transport in planar graphene systems. However, the curvature in the stepped graphene systems can alter their electronic properties, i.e., can induce electron scatterings, especially, when a local strain occur around the step edges as discussed above. Hence, the validity of the  $p_z$  TB model is needed to be examined. To this aim, we performed quantum transport calculations based on density functional theory (DFT) [6] for stepped graphene systems, which are assumed very large so as to neglect the finite-width effects and hence the periodic boundary condition can be applied along Oy axis.

The transmission coefficients through stepped graphene systems obtained for three different  $k_y$ -momentum modes around the Dirac point are computed and presented in Fig. S2. Two cases without and with a local strain ( $\epsilon_{\max} = 1\%$ ) are considered. In agreement with the study in [7] with different curvature radius, step heights and step angles, the results obtained without the local in-plane strain show that the effects of curvature on the electronic transport through the system is negligible. In particular, for  $k_y = K_0$ , the transmission coefficient exhibits only negligibly small reduction around the zero energy point, compared to the planar case where it is unity and constant in the considered energy range. Thus, the curvature does not induce significant electron scatterings and hence, similar to the planar cases, the  $p_z$  TB Hamiltonian still works well for these considered stepped graphene systems.

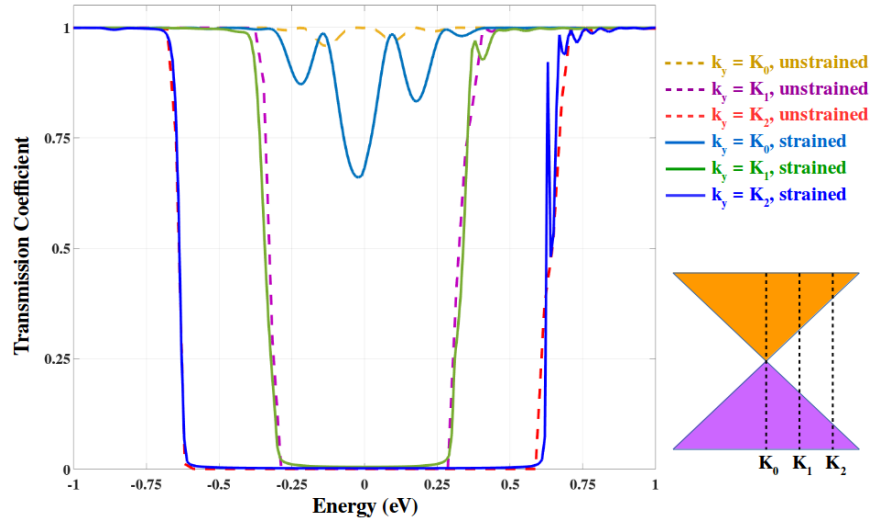


**Fig. S2:** Electronic transport through stepped 2D graphene systems using DFT calculations: strained (with  $\epsilon_{\max} = 1\%$ ) system as described in Fig.S1 versus unstrained one.

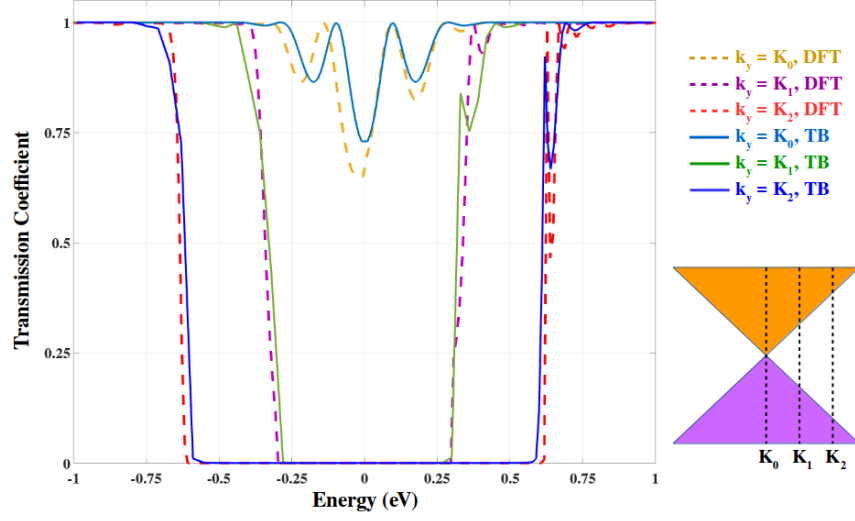


**Fig. S3:** Electronic transport through stepped 2D graphene system with local strain  $\epsilon_{\max} = 1\%$ : Tight-Binding vs DFT calculations.

When the curvature-induced local strains are introduced, significant electron scatterings at the step edges can be observed. Indeed, the transmission coefficient exhibits significant reduction around the zero energy point for  $k_y = K_0$  mode and close to the edges of energy gap for other modes  $K_{1,2}$ . In order to compute these effects, the  $p_z$  TB Hamiltonian must be adjusted. In particular, a model where the hopping term is determined a function of C-C bond length  $r_{ij}$  as  $t_{ij} = t_0 \exp[\beta(1 - r_{ij}/r_0)]$  with  $\beta = 3.37$  and  $r_0 = 0.142$  nm has been demonstrated [8] to compute well the strain effects in graphene. Fig. S3 demonstrates a quite good agreement between the DFT data and results obtained by such strained TB model. Our calculations show that this strained TB Hamiltonian without any other adjustment is still a good model for the considered stepped graphene systems with local strains of  $\epsilon_{\max} \lesssim 4\%$ .

#### 4. Effects of curvature-induced local strains on Aharonov-Bohm interference

In this section, we employed the strained TB model presented above to investigate the effects of curvature-induced local strains in the Aharonov-Bohm interferometers predicted in this work.

The conductance as a function of Fermi energy obtained at zero magnetic field is presented in Fig. S4. Similar to the results presented in section 3, the considered local strain can induce electron scatterings and affect significantly the transport through the system, leading to the conductance reduction.

The effects of such strains on the predicted Aharonov-Bohm interference are investigated and presented in Fig. S5. It is however shown that the effects on the conductance oscillations in the quantum Hall regime are relatively weaker than those observed in the low field one. This can be explained as follows. In the low field regime, the electron transport is essentially due to “bulk states”, which transmit across the step edges (i.e., zones of local strains) and hence undergo strong back-scatterings as described in the top-right image of Fig.S5. In the quantum Hall regime, the presence of these locally strained zones however affects the transport picture differently. In particular, when a high magnetic field with  $\theta_B < \theta_s$  is applied, opposite edge states are formed in terrace and facet zones (in two sides of the step edges) and electrons transmitting through the system have to follow trajectories as described in the bottom-

right image of Fig.S5, i.e., when reaching the step edges, electrons transmit along (not directly across, as in the zero-field case) these edges. This can eliminate the scatterings induced by the considered local strains and explain their weak effects in the quantum Hall regime, compared to those in the low field one. Hence, within the range of experimentally reported strains discussed above, the considered local strains even though alter but does not strongly perturb the predicted Aharonov-Bohm interference.

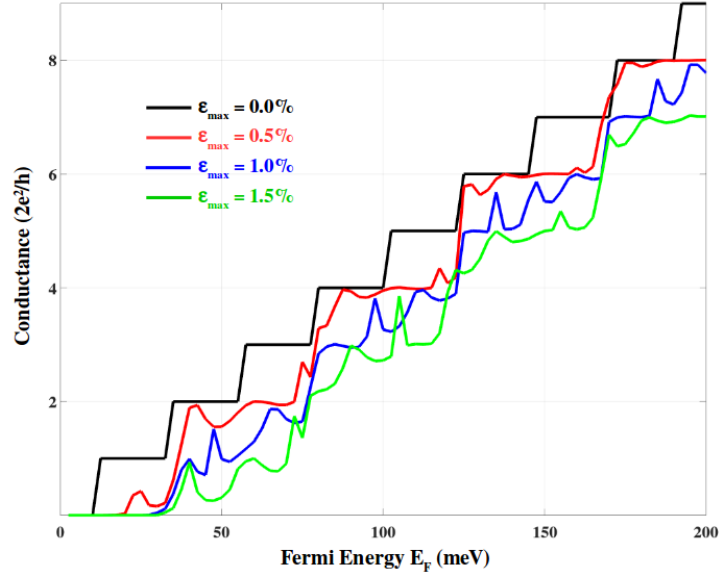


**Fig. S4:** Conductance as a function of energy at zero magnetic field with different curvature-induced strains. The strain release distance  $d_0 \approx 11$  nm while other parameters are as in Fig.2 of the main text.

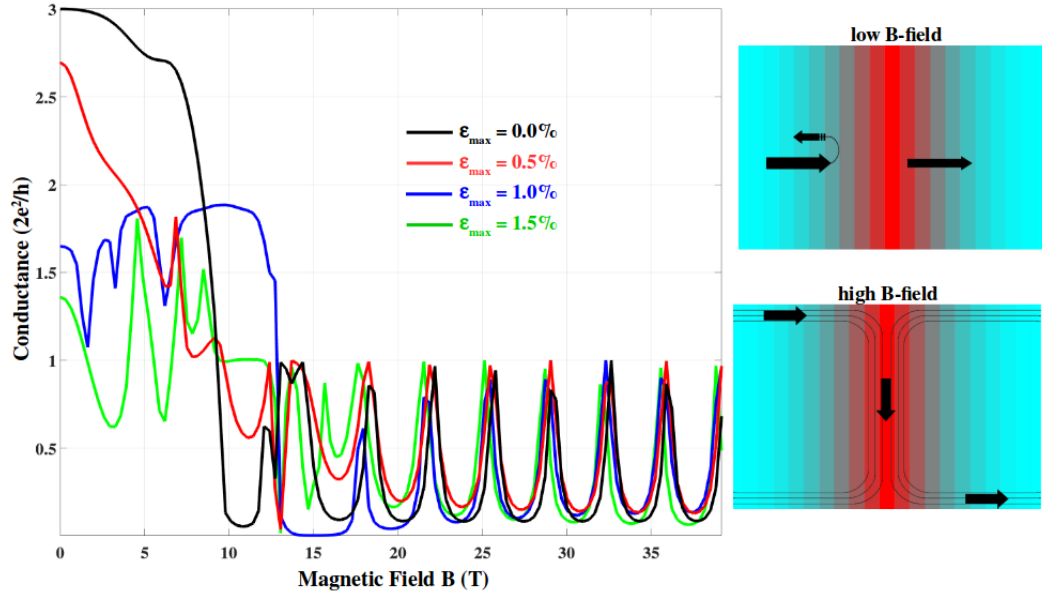


**Fig. S5:** Conductance as a function of magnetic field at  $E_F = 75$  meV and with different curvature-induced strains. Parameters are as in Fig.S4. Right panels illustrate the electron transport pictures at low and high magnetic fields.

Certainly, the effects of these local strains on the Aharonov-Bohm interference can be enlarged and significant when much larger strain gradients occur, for instance, when external stresses are additionally applied.

## 5. Effects of edge disorder in graphene nanoribbons

Similar to the surface roughness in many nanoscale systems of conventional semiconductors, the edge disorder (i.e., edge roughness) is often a practical issue for graphene ribbons [9-19]. The edge disorder has been shown to affect strongly the electronic transport through graphene ribbons, especially, when their width reaches the nanoscale regime.

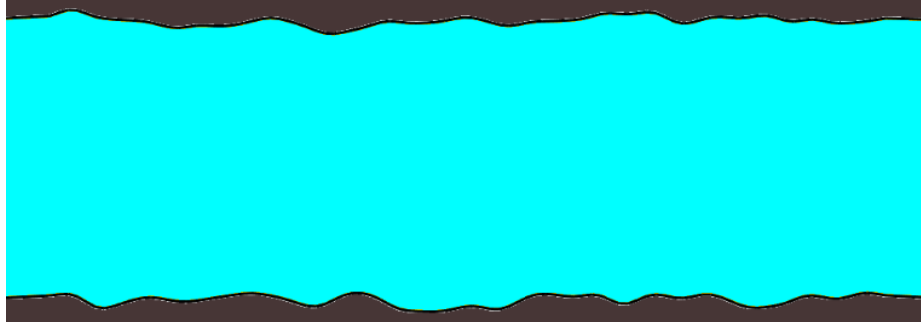


**Fig. S6:** *Graphene ribbon with edge disorder.*

To investigate the effects of edge disorder, there were two models widely used in the literature. In particular, the disordered edges can either be generated by randomly removing the edge atoms with a certain probability [11-14] or are modeled using auto-correlation functions [15-19]. These models have been demonstrated to interpret well the electronic properties of GNRs in experiments with a wide range of disorder level [9-19]. Here, the effects of edge disorder are examined using both two models. In the latter case, the edge disorder is generated by a Gaussian autocorrelation function, particularly, the variation of ribbon width  $\delta W$  is effectively described as

$$\langle \delta W(x) \delta W(x + \Delta x) \rangle = W_{rms}^2 \exp\left(-\frac{\Delta x^2}{2\xi^2}\right) \quad (S.6)$$

where  $W_{rms}$  is the rms value characterizing the disorder strength and  $\xi$  represents the correlation length.

A typical picture of edge disordered graphene ribbons is illustrated in Fig. S6. The effects of edge disorder generated by a Gaussian autocorrelation function are presented in Fig. 4 of the main text and the results obtained in the systems by randomly removing edge atoms are displayed in Fig. S7.

### **Actually, two main features are found with both disorder models.**

First, in the case of semiconducting GNRs, the Aharonov-Bohm oscillations obtained at high magnetic fields ( $B$ -fields) are shown to be much more robust under the effect of the considered disorders than the zero-field transport. This can be explained by a fascinating feature that different from the zero-field case (see Figs.S8 (a,d)), the forward and backward edge channels are spatially separated in the quantum Hall regime (see Figs.S8 (b-c, e-f)) while the scatterings at the disordered edges do not allow electrons

to transmit across the sample. As a consequence, the edge disorder effects do not contribute significantly to backscatterings in the considered stepped systems, i.e., the dominant mechanism of backscattering is still interaction between edge states in zones of opposite normal  $B$ -fields and hence strong Aharonov-Bohm oscillations are still achieved.

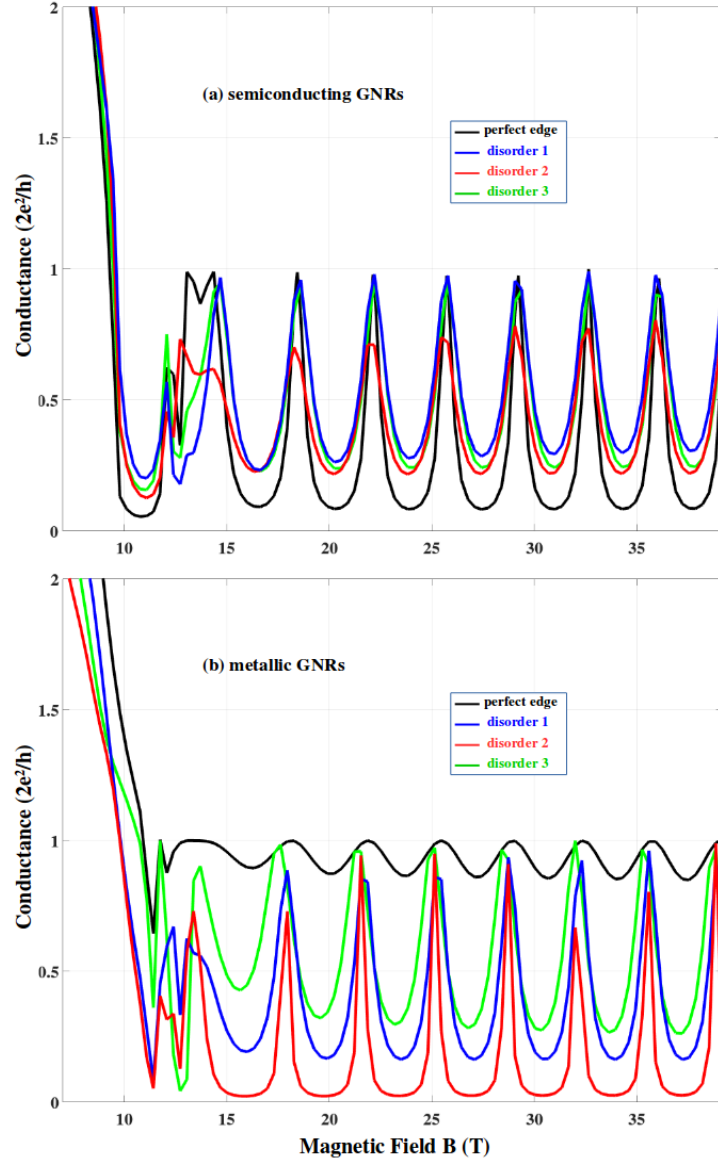


**Fig. S7:** (a,b) Conductance as a function of  $B$ -field at  $E_F = 75$  meV computed for semiconducting ( $N_z = 324$ ) and metallic ( $N_z = 326$ ) GNR systems, respectively, with  $\theta_s = 60^\circ$ ,  $\theta_B = 30^\circ$ ,  $L_F \approx 75$  nm and  $W \approx 40$  nm. In the edge disordered systems, 15% of edge atoms are randomly removed.

Second, as presented in Fig.4 of the main text and in Fig. S7, there is a significant difference between semiconducting and metallic GNR systems with perfect edges, i.e., the Aharonov-Bohm oscillation is relatively weak in the metallic cases, compared to the results obtained in semiconducting ones. The



edge disorder however strengthens the Aharonov-Bohm oscillation in metallic GNR systems, thus eliminating the difference mentioned.

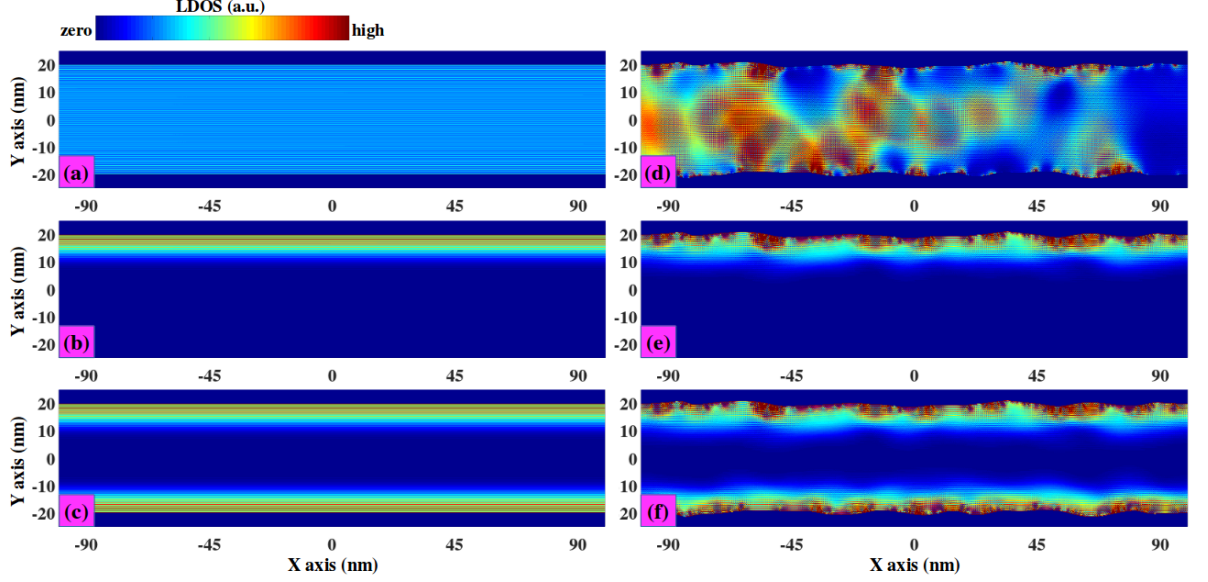


**Fig. S8:** Edge disorder effects on electron propagation in planar graphene ribbons: left-injected LDOS (a,b,d,e) and total LDOS (c,f). Magnetic fields  $B = 0$  in (a,d) and  $25$  T in (b,c,e,f) while carrier energy  $E = 75$  meV. Perfect and disordered edges are considered in (a,b,c) and (d,e,f), respectively.

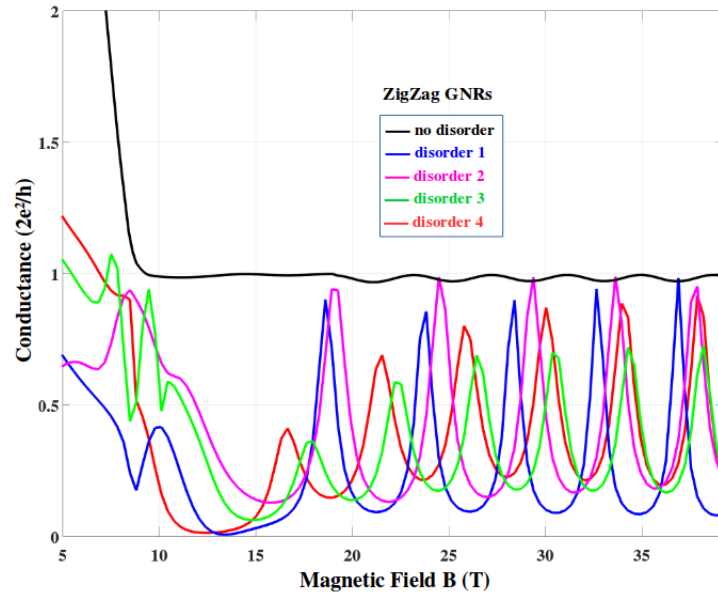


**Fig. S9:** Conductance as a function of B-field at  $E_F = 75$  meV obtained in stepped systems of a zigzag GNR with  $\theta_S = 60^\circ$ ,  $\theta_B = 30^\circ$ ,  $L_F \approx 72$  nm and  $W \approx 40$  nm. The disordered edge systems are generated by the Gaussian autocorrelation function (S.6) with  $W_{rms} \approx 0.6$  nm and  $\xi \approx 4.8$  nm.

Note additionally that a picture, similar to those obtained in the metallic armchair GNRs, is also observed in zigzag GNR systems, i.e., the Aharonov-Bohm oscillation is relatively weak for perfect edges but the effect is much more pronounced when edge disorder is introduced (see Fig. S9).

## 6. Multi sub-bands contribution

In this section, we analyze the effects of multi sub-bands contribution on the predicted Aharonov-Bohm oscillation in more detail. As it has been demonstrated in nanorings [20,21] and also in graphene  $p$ - $n$  junctions [22], the Aharonov-Bohm interference has an inherent property that the strong oscillation of conductance can be observed in the low energy regime where only a single band is obtained. In the regime of high energies when multi energy bands can contribute to the transport, the interference picture can be significantly blurred. A similar feature is also observed in the Aharonov-Bohm interferometers considered here.

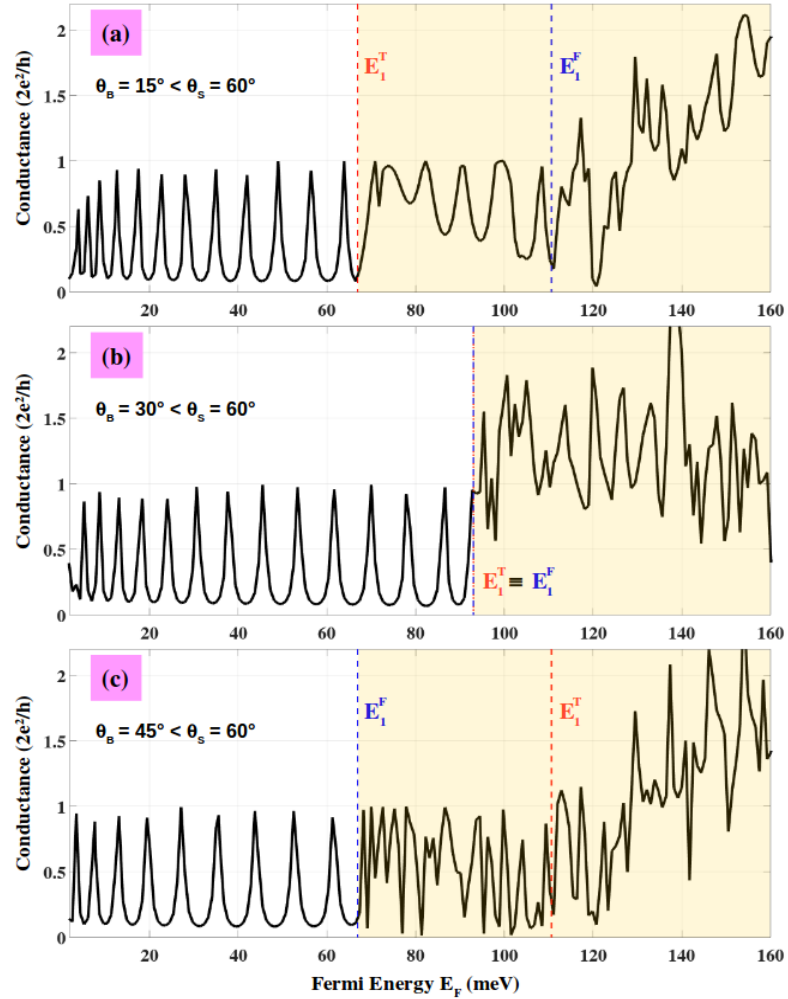


**Fig. S10:** Conductance as a function of Fermi energy at  $B = 20$  T obtained in stepped systems of an armchair GNR with  $L_F \approx 110$  nm and  $W \approx 60$  nm. The stepped angle  $\theta_s = 60^\circ$  while three directions of B-field are considered.  $E_1^{T(F)}$  indicates the first Landau level formed in the terrace (facet) zone.

Indeed, as shown in Fig. S10 and Fig. 5 of the main text, strong conductance oscillations in all considered cases are observed in the regime  $E_F \leq \min(E_1^T, E_1^F)$  where  $E_1^{T,F}$  are the first Landau levels formed in the terrace and facet zones, respectively, at high magnetic fields. In Fig. S11, the energy bands of an armchair GNR under the effect of magnetic field are presented. When a high magnetic field is applied, the energy bands of GNR are strongly modified and the Landau quantization is observed as seen in the right panel of Fig.S11. This Landau quantization (i.e., energy levels  $E_{0,\pm 1,\pm 2,\dots}$ ) obeys the well-known formula [23]

$$E_n = \text{sign}(n) \sqrt{2e\hbar v_F^2 |n| B_\perp} \quad (\text{S.7})$$

where  $v_F$  is the Fermi velocity in graphene. The energy levels  $E_1^T$  and  $E_1^F$  mentioned above are hence determined as  $E_1^T = \sqrt{2e\hbar v_F^2 B |\sin \theta_B|}$  and  $E_1^F = \sqrt{2e\hbar v_F^2 B |\sin(\theta_S - \theta_B)|}$ .

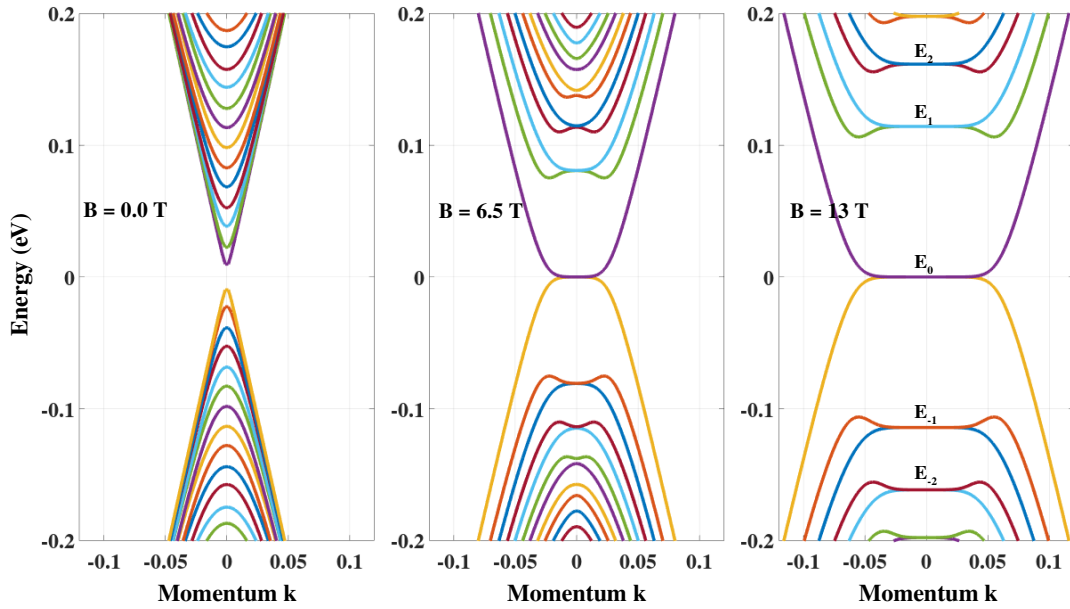


**Fig. S11:** Energy bands of the armchair GNR of  $W \approx 60$  nm under the effect of magnetic field. Energy levels  $E_n$  ( $n=0,\pm 1,\pm 2,\dots$ ) in the right panel represent the Landau quantization at a high B-field [23].

In the high energy regime, the effects of multi sub-bands contribution, similar to those observed in graphene and phosphorene nanorings [20,21] and mentioned above, are clearly demonstrated in Fig.S10 (see the zones highlighted in yellow). In general, the Aharonov-Bohm oscillations are significantly blurred by such contribution when  $E_F > \min(E_1^T, E_1^F)$ , as illustrated in both Fig. S10 here and Fig.5 of the main text. In the cases if  $E_1^T \neq E_1^F$  (e.g.,  $\theta_B = 15^\circ$  and  $45^\circ$ ), some oscillations can still be well defined in the range between these two values (see Fig. S10 for  $\theta_B = 15^\circ$ ).

The features presented here explain clearly the results presented and discussed in Fig.5 of the main text.

## References:

- [1] V. Hung Nguyen *et al.*, J. Comput. Electron. **12**, 85-93 (2013).
- [2] C. H. Lewenkopf and E. R. Mucciolo, J. Comput. Electron. **12**, 203-231 (2013).
- [3] J. A. Robinson *et al.*, Nano Lett. **9**, 964-968 (2009).
- [4] T. Low, V. Perebeinos, J. Tersoff, and Ph. Avouris, Phys. Rev. Lett. **108**, 096601 (2012).
- [5] B. D. Briggs *et al.*, Appl. Phys. Lett. **97**, 223102 (2010).
- [6] <http://www.openmx-square.org>
- [7] Y. Xu, H. Gao, M. Li, Z. Guo, H. Chen, Z. Jin and B. Yu, Nanotechnol. **22**, 365202 (2011).
- [8] V. M. Pereira, A. H. Castro Neto, and N. M. R. Peres, Phys. Rev. B **80**, 045401 (2009).
- [9] M. Y. Han, B. Özyilmaz, Y. Zhang, and P. Kim, Phys. Rev. Lett. **98**, 206805 (2007).
- [10] M. Y. Han, J. C. Brant, and P. Kim, Phys. Rev. Lett. **104**, 056801 (2010).
- [11] M. Evaldsson *et al.*, Phys. Rev. B **78**, 161407(R) (2008).
- [12] D. Querlioz *et al.*, Appl. Phys. Lett. **92**, 042108 (2008).
- [13] A. Cresti and S. Roche, New J. Phys. **11**, 095004 (2009).
- [14] M. Poljak and T. Suligoj, IEEE Trans. Electron Devices **63**, 537-543 (2016).
- [15] M. V. Fischetti and S. Narayanan, J. Appl. Phys. **110**, 083713 (2011).
- [16] N. Djavid *et al.*, IEEE Trans. Electron Devices **61**, 23 - 29 (2014).
- [17] T. Misawa *et al.*, Jpn. J. Appl. Phys. **54**, 05EB01 (2015).
- [18] T. Fang, A. Konar, H. Xing, and D. Jena, Phys. Rev. B **78**, 205403 (2008).
- [19] A. Y. Goharrizi *et al.*, IEEE Trans. Electron Devices **58**, 3725 - 3735 (2011).
- [20] V. Hung Nguyen, Y. M. Niquet, and P. Dollfus, Phys. Rev. B **88**, 035408 (2013).
- [21] R. Zhang, Z. Wu, X. J. Li, and K. Chang, Phys. Rev. B **95**, 125418 (2017).
- [22] A. Mreńca-Kolasińska, S. Heun, and B. Szafran, Phys. Rev. B **93**, 125411 (2016).
- [23] L.-J. Yin, K.-K. Bai, W.-X. Wang, S.-Y. Li, Y. Zhang, and L. He, Front. Phys. **12**, 127208 (2017).